International Journal of Coal Science & Technology (2025) 12:23
https://doi.org/10.1007/s40789-025-00748-7

RESEARCH

An efficient coal and gas outburst hazard prediction method using an improved limit equilibrium model and stress field detection

Yingjie Zhao[1,2] · Dazhao Song[1,2] · Liming Qiu[1,2] · Majid Khan[1,2] · Xueqiu He[1,2,3] · Zhenlei Li[1,2] · Yujie Peng[1,2] · Anhu Wang[1,2]

Received: 17 August 2023 / Revised: 26 March 2024 / Accepted: 2 January 2025

Abstract
Accurate prediction of coal and gas outburst (CGO) hazards is paramount in gas disaster prevention and control. This paper endeavors to overcome the constraints posed by traditional prediction indexes when dealing with CGO incidents under low gas pressure conditions. In pursuit of this objective, we have studied and established a mechanical model of the working face under abnormal stress and the excitation energy conditions of CGO, and proposed a method for predicting the risk of CGO under abnormal stress. On site application verification shows that when a strong outburst hazard level prediction is issued, there is a high possibility of outburst disasters occurring. In one of the three locations where we predicted strong outburst hazards, a small outburst occurred, and the accuracy of the prediction was higher than the traditional drilling cuttings index S and drilling cuttings gas desorption index q. Finally, we discuss the mechanism of CGO under the action of stress anomalies. Based on the analysis of stress distribution changes and energy accumulation characteristics of coal under abnormal stress, this article believes that the increase in outburst risk caused by high stress abnormal gradient is mainly due to two reasons: (1) The high stress abnormal gradient leads to an increase in the plastic zone of the coal seam. After the working face advances, it indirectly leads to an increase in the gas expansion energy that can be released from the coal seam before reaching a new stress equilibrium. (2) Abnormal stress leads to increased peak stress of coal body in front of working face. When coal body in elastic area transforms to plastic area, its failure speed is accelerated, which induces accelerated gas desorption and aggravates the risk of outburst.

Keywords Coal and gas outburst · Mechanical model · Instability · Seismic wave tomography · Prediction method

1 Introduction

Coal and gas outbursts (CGO) pose a complex and multifaceted coupling disaster in coal mining, with China being the country most severely affected by this phenomenon worldwide. Over the period from January 2012 to April 2022, China encountered 101 CGO incidents, tragically resulting in 689 fatalities (Zhang et al 2021). Despite extensive research efforts by scholars both domestically and internationally, the underlying mechanism of CGO remains incompletely understood. Several hypotheses have been proposed to elucidate this phenomenon, with the CGO comprehensive action hypothesis garnering widespread recognition. This hypothesis takes into account the combined effects of stress, gas pressure, and the inherent characteristics of coal to explain CGO occurrences (Li et al 2017; Wold et al 2008). Some scholars categorized the entire process of CGO into four stages: incubation, stimulation, development, and termination (Cao et al 2019; Wang et al 2018b, a). They asserted that the stress state of the coal body plays a dominant role in the preparation stage for outburst incubation. As research on relevant mechanisms continues to deepen, scholars have provided detailed insights into the specific process of CGO from various perspectives, including stress and gas. These perspectives encompass the stress state of coal (Shu et al 2023; Lu et al 2017), structural characteristics (Tian et al 2021; Zhang et al 2011), failure morphology (Pan et al 2020), gas adsorption analysis characteristics (Sobczyk

✉ Dazhao Song
songdz@ustb.edu.cn

[1] School of Civil and Resources Engineering, University of Science and Technology Beijing, Beijing 100083, China

[2] Key Laboratory of Ministry of Education for Efficient Mining and Safety of Metal Mine, University of Science & Technology Beijing, Beijing 100083, China

[3] Zhong-an Academy of Safety Engineering, Beijing, China

Published online: 07 March 2025

2014; Black 2019), and seepage characteristics (Peng et al. 2012), among others.

In recent years, as mining operations have been carried out at greater depths, the occurrence of coal and gas outbursts, along with abnormal gas emission accidents, has shown an upward trend. Notably, these incidents have been observed even when the gas pressure, content, and other related indicators are lower than the traditional threshold values associated with coal and gas outbursts (Liu et al. 2021). Research indicates that CGO frequently occurs during tunnel excavation, particularly in the southwestern region of China, where coal seams are densely distributed in local structural areas like synclines, anticlines, and approximately parallel faults and fold combinations (Chen et al. 2023). These geological features induce substantial stress changes, leading to a more intricate distribution of stress fields (Kong et al. 2022).

For stress anomalies caused by non excavation disturbances such as coal rock depth, folds, faults, sudden changes in coal seam thickness, and hidden structures, we define them as non excavation disturbance stress anomalies (NEDSA). When the working face advances near NEDSA, the distribution of excavation disturbance stress will undergo significant changes. Failing to consider the impact of non-excavation disturbance stress anomaly (NEDSA) tends to elevate the hazard of CGO accidents (Li et al 2022, 2018; Wang 2017). Currently, modeling and numerical simulation of local structural regions, such as known faults, folds, and tectonic coals, is a common approach in studying the effects of stress anomalies on CGOs, which plays an important role in advancing the study of prominence hazard prediction (Xu et al2006; Soleimani et al 2023a, 2023b). However, the numerical simulation method is limited when there are unknown hidden structures or faults within the coal rock body. Another principal approach entails analyzing analytical expressions (Xue et al 2014), which, however, may not fully account for the influence of abnormal stress distribution—a critical factor in the analysis. There is a lack of studies focusing on predicting CGO hazards in excavation tunnels using NEDSA detection results. Therefore, the pivotal aspect of advancing disaster prevention efforts lies in developing a forward-facing mechanical model, investigating the influence of NEDSA on the incubation and initiation process of CGO, and formulating appropriate CGO disaster hazard prediction methods. Wang et al (2019) and Zhao et al (2023) successfully detected geological anomalies in the excavation tunnel area of outburst mines by installing micro-seismic (MS) monitoring equipment and utilizing seismic wave tomography technology. This provides valuable support for conducting CGO hazard analysis considering NEDSA.

In summary, this study established a mechanical model for the front of the protruding coal seam working face under abnormal stress. Furthermore, an analysis of the excitation conditions of CGO in the excavation roadway was conducted, leading to the establishment of a CGO hazard prediction method employing seismic wave tomography technology. The practical application and validation of this method were performed on-site, yielding promising results. The research results of this article are of great significance for the safe and efficient promotion of prominent coal seams and improving the accuracy of CGO hazard prediction. Finally, the mechanism of coal and gas outburst under stress was discussed.

2 Improved mechanical model of coal roadway excavation

2.1 Basic assumptions and boundary conditions

Initially, the coal body bears the action of the overlying load σ_y in its undisturbed state. Indeed, following the excavation of the coal roadway, the overlying load gradually transfers to the front coal body, ultimately leading to a state of stability. Figure 1 depicts a schematic diagram of the stress distribution in front of the tunnel, both in the absence and presence of NEDSA. It is evident that when NEDSA is present in front of the tunnel, it can easily cause the coal seam to reach its ultimate bearing capacity and become unstable, thereby leading to coal and gas outburst accidents. Consequently, establishing a mechanical model for the instability of gas-bearing coal seams, considering the influence of NEDSA, is of paramount importance for predicting CGO hazards. To simplify the research, given the complex mechanical properties of coal, we make the following assumptions:

(1) The coal rock mass is considered a uniform, continuous, and isotropic elastic–plastic body, with the elastic zone of the coal body satisfying Hooke's law.
(2) The friction coefficient between the roadway and the roof and floor is assumed to be the same, and the self-weight of the coal seam is neglected.
(3) The temperature stress field is not taken into consideration.
(4) Differences in internal friction angle and cohesion between weak surfaces with low stability among coal and rock masses, as well as between coal seams within the coal body, have not been accounted for in the analysis.
(5) Stress in the inclined direction of the working face is disregarded.

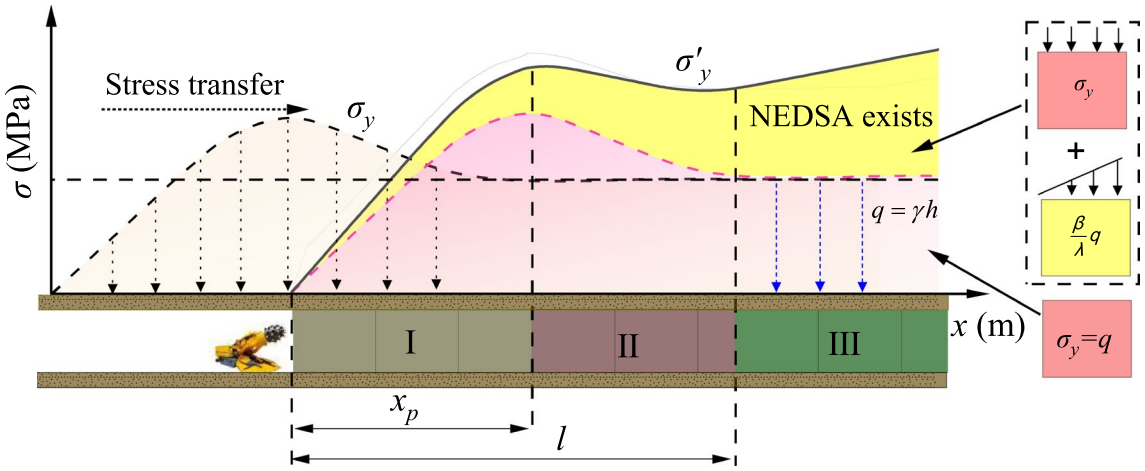

Fig. 1 Schematic diagram of stress distribution in excavation tunnels: I, II, and III represent plastic zone, elastic zone, and original rock stress zone, respectively; x_p is the length of the plastic zone, l is the length of the disturbance zone, λ is the lateral pressure coefficient, β is the NEDSA coefficient

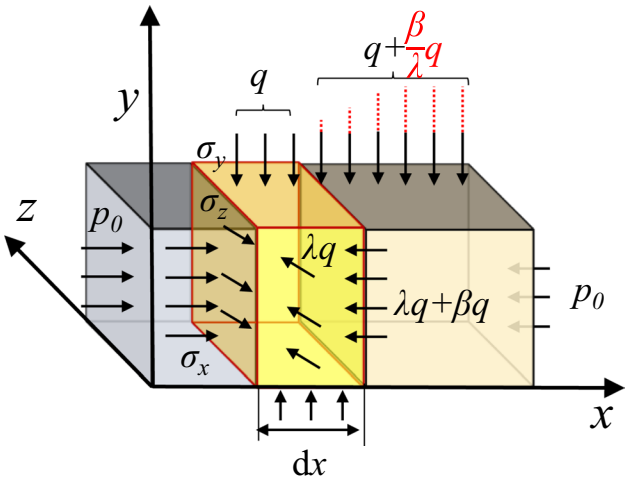

Fig. 2 Micro-element force analysis of different areas in front of the tunnel face

2.2 Equilibrium equation for the original rock stress zone

As illustrated in Fig. 2, a small unit is carefully extracted from within the original rock stress zone. Owing to the mutual constraints on the coal body, lateral deformation remains minimal, giving rise to lateral pressure in the horizontal direction. When NEDSA exists, it is also subjected to βq stress in the horizontal direction.

For gas-containing coal seams, the total stress on the coal body is generally expressed as effective stress (Xu et al 2006):

$$\sigma_m = \sigma_{me} + \alpha p \tag{1}$$

where σ_m is the total stress, MPa; σ_{me} is effective stress, MPa; α is the effective stress coefficient; p is the coal seam gas pressure, MPa.

Studies have shown that the gas pressure gradient is higher near the coal wall of the working face and gradually decreases with increasing distance (Wang et al 2018b, a). The following exponential function can represent the dynamic distribution curve of gas pressure:

$$p = p_0(1 - e^{-Ax}) \tag{2}$$

where p is the gas pressure, MPa; p_0 is the initial gas pressure, MPa; x is the distance from the coal wall of the working face, m; A is the coefficient constant.

The horizontal lateral pressure coefficient (λ) generated by the vertical load is:

$$\lambda = \frac{\sigma_x}{\sigma_y} = \frac{\mu}{1-\mu} \tag{3}$$

where σ_x is the horizontal stress, σ_y is the vertical stress, and μ is the Poisson's ratio.

The unit body in the original stress zone is subjected to compressive stress generated by the overlying surrounding rock, gas pressure, and NEDSA. The components in the y-axis direction are as follows:

$$\begin{cases} \sigma_y = (1 + \dfrac{\beta_2}{\lambda})q + \alpha p \\ q = \gamma h \end{cases} \tag{4}$$

where q is the overlying load in the primary rock stress zone without NEDSA. γ is the bulk density of coal and rock mass. h is the buried depth of coal and rock; β_2 is the NEDSA

coefficient at the junction of the plastic zone and the original rock stress zone.

The original rock stress zone remains unaffected by excavation disturbance, so the gas pressure in this zone is the original gas pressure p_0. Combining formulas (3) and (4), the stress balance equation of the unit body with a height of m in the original stress zone is as follows:

$$m\sigma_x + mp_0 = m(\lambda q + \beta_2 q) + mp_0 \tag{5}$$

Combining formulas (4) and (5), the horizontal and vertical stresses of the coal seam in the original stress zone under the influence of NEDSA and gas pressure are as follows:

$$\begin{cases} \sigma_x = \lambda q + \beta_2 q + \alpha p_0 \\ \sigma_y = q + \dfrac{\beta_2}{\lambda} q + \alpha p_0 \end{cases} \tag{6}$$

2.3 Equilibrium equation for the elastic region

The stress calculation models for the elastic zone encompass limit equilibrium models and spherical shell instability models, both of which are extensively employed in analyzing the mechanics of CGO developments. The stress calculation in the elastic zone using the limit equilibrium model relies on knowledge of the stress concentration coefficient for solving the length of the plastic zone. To overcome this limitation, this article introduces the instability model of the spherical shell to establish a stress state model in the elastic zone, effectively considering the influence of NEDSA. The instability model of the spherical shell assumes a spherical shape for the excavation face, and Fig. 3 illustrates the stress state of the micro-element body in the elastic zone (Jiang et al. 1998).

The force balance equation can be expressed as follows due to the equal magnitude of tangential stress in the micro-element body (Jiang et al. 1998):

$$\begin{aligned} &\left[\sigma_r + \alpha p\right] r^2 \mathrm{d}\theta^2 - \left[(\sigma_r + \mathrm{d}\sigma_r) + \alpha p\right](r + \mathrm{d}r)^2 \mathrm{d}\theta^2 \\ &+ 4\left[\sigma_t + \alpha p\right] r \mathrm{d}r \mathrm{d}\theta \cdot \sin\frac{\mathrm{d}\theta}{2} = 0 \end{aligned} \tag{7}$$

where σ_t is tangential stress, MPa; σ_r is radial stress, MPa; r is the particle radius, m; θ is the micro coordinate Angle, and α is the effective stress coefficient.

After expanding the above equation and simplifying the solution, the following conclusion can be drawn:

$$\begin{cases} \sigma_{rw} = \dfrac{B}{r^3} + P + \alpha p \\ \sigma_{tw} = -\dfrac{B}{2r^3} + P + \alpha p \end{cases} \tag{8}$$

where B is the constant to be determined and P is the original rock stress, MPa.

Combining formula (6), we can draw the following conclusion:

$$\begin{cases} \sigma_{tw} = -\dfrac{B}{2r^3} + (1 + \dfrac{\beta_2}{\lambda})q + \alpha p \\ \sigma_{rw} = \dfrac{B}{r^3} + (\lambda + \beta_2)q + \alpha p \end{cases} \tag{9}$$

2.4 Equilibrium equation for plastic zone

Here, we investigate the stress state within the plastic zone, incorporating the influence of NEDSA using the limit equilibrium model, as the stress state calculation in this region

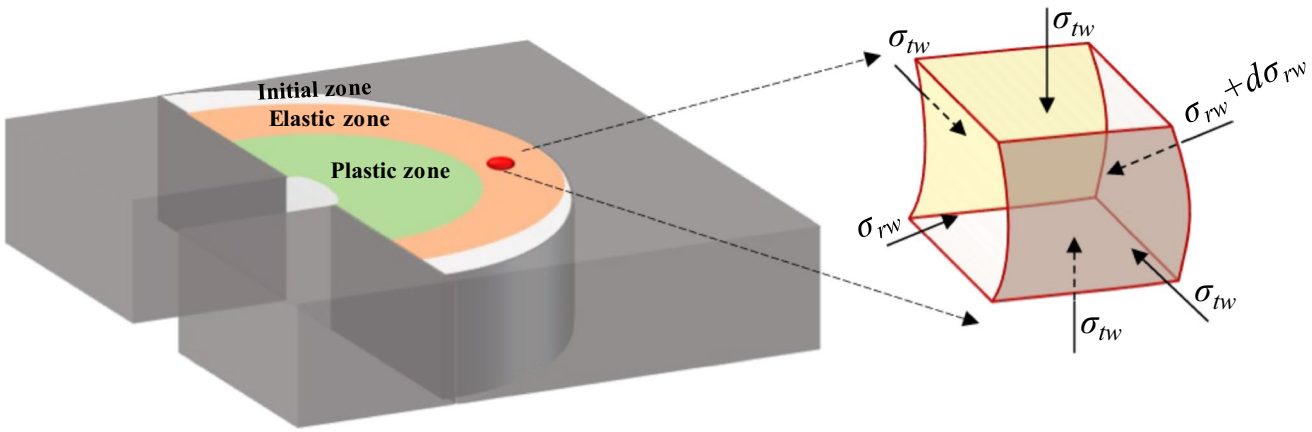

Fig. 3 Stress Analysis of Micro-element body in Elastic Zone

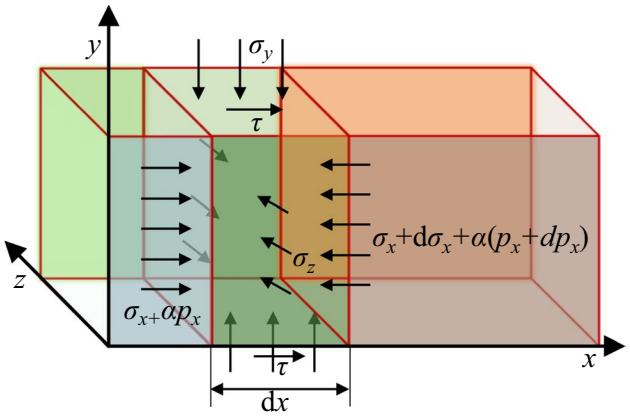

Fig. 4 Stress analysis of microelement in the plastic zone

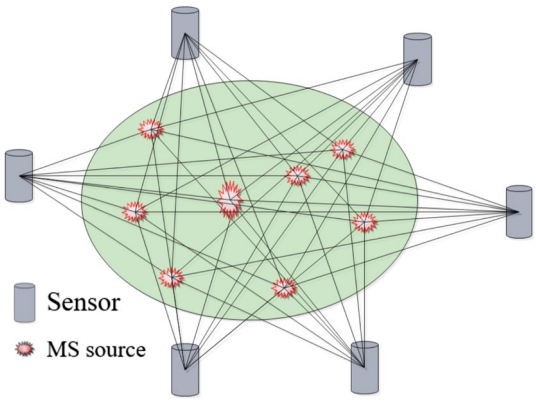

Fig. 5 Schematic diagram of seismic wave tomography imaging

aligns more closely with the characteristics of this particular model. The stress state of the plastic zone is depicted in Fig. 4.

As x increases, the horizontal stress on the micro-element body gradually increases. To ensure force balance, the friction force (τ) acting on the micro-element body should be in the positive direction of the x-axis, and its calculation formula is as follows:

$$\tau = f\left(\sigma_y + \sigma_z\right) + 2c_0 \tag{10}$$

where f is the friction coefficient between the top and bottom plates and the coal, its value is tanφ, φ is the internal friction angle of the coal seam, and c_0 is the cohesive force.

The horizontal stress equilibrium equation of the plastic zone unit is as follows (Jia et al 2011):

$$\frac{\mathrm{d}\sigma_x}{\mathrm{d}x} + \frac{\alpha \mathrm{d}p}{\mathrm{d}x} = \frac{2f}{m}\left(\sigma_y + \sigma_z\right) + \frac{4c_0}{m} \tag{11}$$

Since coal bodies in the plastic zone often exhibit elastic-brittle behavior after failure, the ultimate equilibrium conditions in the plastic zone are governed by the M-C (Mohr–Coulomb) criterion:

$$\begin{cases} \sigma_y = k\sigma_x + \sigma_c \\ k = \dfrac{1+\sin a}{1-\sin a} \end{cases} \tag{12}$$

Assuming that the coal wall is unsupported, when $x=0$, the boundary conditions are as follows:

$$\begin{cases} \sigma_x = -\beta_1 q \\ p = 0 \end{cases} \tag{13}$$

where, β_1 is the NEDSA coefficient at the heading coal wall of the excavation.

Under the influence of NEDSA, the horizontal and vertical stresses of coal seams in the plastic zone are as follows in the simultaneous solution formulas (10) to (13):

$$\begin{cases} \sigma_x = \left(\dfrac{\sigma_c}{k} + \dfrac{2c_0}{k(1+\lambda)f}\right)\left(e^{\frac{2fk(1+\lambda)}{m}x} - 1\right) - \dfrac{\alpha p_0\left(e^{\frac{2fk(1+\lambda)}{m}x} - e^{-\frac{2fk(1+\lambda)}{m}x}\right)}{2} + \beta_1 q e^{\frac{2fk(1+\lambda)}{m}x} \\ \sigma_y = k\left[\sigma_x - \alpha p_0\left(1 - e^{\frac{-2fk(1+\lambda)}{m}x}\right)\right] + \sigma_c + \alpha p_0\left(1 - e^{\frac{-2fk(1+\lambda)}{m}x}\right) \end{cases} \tag{14}$$

CGO incubation and excitation generally occur within the plastic zone; therefore, calculating the extent of the plastic zone is crucial for analyzing the hazard of CGO. Since the peak stress is equal at the intersection of the elastic and plastic regions, the value of $x = x_p$ is simultaneously substituted into formulas (9) and (15).

Let $C = 2fk(1+\lambda)/m$; after simplification, we get:

$$T = Ne^{Cx} + Fe^{-Cx} \tag{15}$$

Among them:

$$\begin{cases} T = (2 + \dfrac{2\beta_2}{\lambda} + \lambda + \beta_2)q + \dfrac{\sigma_c}{k} + \dfrac{2c_0}{kf(1+\lambda)} + \dfrac{4c_0}{f(1+\lambda)} + \alpha p_0 + 2\alpha p_0 k \\ N = 2\sigma_c + \dfrac{4c_0}{f(1+\lambda)} + \dfrac{\sigma_c}{k} + \dfrac{2c_0}{kf(1+\lambda)} + 2k\beta_1 q + \beta_1 q - \alpha p_0 k - \dfrac{\alpha p_0}{2} \\ F = 3\alpha p_0 k - \dfrac{3\alpha p_0}{2} \end{cases} \tag{16}$$

By solving the above equation, we can obtain:

$$x_p = \frac{1}{C}\ln\frac{T + \sqrt{T^2 - 4NF}}{2N} = \frac{1}{C}\ln Q \tag{17}$$

where, the constant coefficient B is:

$$B = \left[(\frac{\sigma_c}{k} + \frac{2c_0}{kf(1+\lambda)})(Q-1) + \beta_1 qQ - (\lambda + \beta_2)q - \alpha p_0 - \frac{\alpha p_0}{2}(Q - \frac{1}{Q})\right]\left[\frac{1}{C}\ln Q\right]^3 \tag{18}$$

that the energy source of CGO primarily originates from coal's elastic potential and gas's expansion energy. This energy is mainly dissipated through coal crushing, movement, acoustic, radiant, and thermal energy. The energy dissipation from the elastic potential, vibration, and sound energy of the top and bottom plates are relatively insignificant, making it possible to disregard these factors in the calculations. Consequently, the conditions for CGO excitation can be simplified to Eq. (19):

$$E_e + E_g > W_c + W_t \tag{19}$$

where E_e is the elastic potential in the skeleton of the coal body, E_g is the protrusion potential of the coal body; W_c is the crushing work of the coal body, and W_t is the moving work of the crushed coal.

3 Proposing and validating prediction methods for CGO hazards

Since the process of CGO excitation and development is a process of energy collection and dissipation, in order to quantitatively study the danger of CGO disaster in the tunneling roadway under the action of NEDSA, it is necessary to calculate the energy transformation during the protruding excitation. It is of great significance to carry out CGO excitation energy calculation on the basis of the NEDSA lower working face mechanical model established in Sect. 2 of this paper to improve the accuracy of CGO hazard prediction.

3.1 Excitation conditions of CGO

The energy dissipation process involved in the excitation and development of CGO is deeply analyzed. It examines the energy evolution leading to CGO excitation and quantitatively investigates the likelihood of CGO disasters occurring in excavation tunnels under the influence of NEDSA. Research findings (Zheng 2004; An et al 2019) indicate

(1) Elastic energy $\boldsymbol{E_e}$

The energy generated by the action of geostress exists in two forms: plastic deformation energy and elastic deformation energy. However, only the elastic deformation energy has the capability to be released to perform external work. The elastic potential per unit volume of coal, denoted as E'_e, can be calculated using Eq. (20) (Qian et al 2003). When the tunnel is not in progress, the vertical stress (σ_y) can be obtained from Eq. (9). After the excavation of L m, σ_y can be approximated using the following Eq. (21).

$$E'_e = \frac{(1-2\mu)(1+2\lambda)^2}{6E}\sigma_y^2 \tag{20}$$

where, E is the modulus of elasticity of coal rock, MPa; μ is the Poisson's ratio; λ is the lateral pressure coefficient.

$$\sigma_y = -\frac{B}{2(x_p - L)^3} + (1 + \frac{\beta_2}{\lambda})q = -\frac{B}{2(x_p - L)^3} + A \tag{21}$$

$$E_e = \frac{(1-2\mu)(1+2\lambda)^2}{6E}\left[A^2x + \frac{B^2}{20(L-x_p)^5} + \frac{AB}{2(L-x_p)^2}\right]\Bigg|_0^L \tag{22}$$

(2) Gas expansion work $\boldsymbol{E_g}$

The coal body comprises a significant quantity of free gas and adsorbed gas. Based on the established relationship between gas content and coal seam gas pressure, the amount of gas released from the coal body, parallel to the coal wall with the thickness of dx is (Yu et al 2013):

$$\begin{cases} \mathrm{d}m_g = \rho \int_{p_1}^{p_x} \dfrac{\eta M}{2\nu_m\sqrt{p}}\mathrm{d}p \\ \eta = \dfrac{Q}{\sqrt{p}} \end{cases} \tag{23}$$

where, m_g is the mass of gas released per unit mass of coal when the gas pressure drops by dp, kg/t; M is the mass of gas molecules, kg/kmol; α is the gas content coefficient, m^3/t $MPa^{0.5}$; Q is the gas content per unit volume of coal, m^3/t; p is the gas pressure, MPa; ν_m is the standard condition gas molar volume of gas at standard condition, m^3/kmol; p_x is the gas pressure at the distance x from the coal wall, MPa; p_1 is underground atmospheric pressure, MPa.

The process of CGO is a variable and dynamic phenomenon, and according to thermodynamic theory, it involves the accomplishment of gas expansion work when the gas pressure of a unit-thickness coal body parallel to the coal wall decreases from p_x to p_1 is:

$$E_g = \frac{\rho\eta M R_g T}{\nu_m(n-1)}\left[1-\left(\frac{P_1}{P_x}\right)^{\frac{n-1}{n}}\right](\sqrt{p_x}-\sqrt{p_1})\mathrm{d}x \tag{24}$$

where E_g is gas expansion work per unit mass, kJ/kg; T is the temperature before gas expansion, K; R is the gas constant, kJ/kg K; n is the gas variable index; ρ is the density of coal t/m^3.

(3) Crushing power $\boldsymbol{W_c}$

The crushing work (W_c) of coal primarily refers to the surface energy required for the newly increased surface area resulting from the coal being crushed into a specific block size. Experimental studies have revealed that the quantity of crushing work needed to generate a unit of new surface area is independent of the magnitude of crushing work and solely depends on coal's physical and mechanical properties. Unit volume coal's crushing work ratio is directly proportional to the consistent coefficient (Cai et al 2005). Therefore, the expression for the crushing work of coal can be simplified as follows:

$$W_c = 10.43\times10^{-3} f x_p s_b \rho \tag{25}$$

where, W_c is the crushing work of the outburst coal body, MJ; w is the crushing specific work of coal J/cm^2; f is the consistent coefficient of coal. s_b is the newly added specific surface area, cm^2/g.

(4) Throwing work $\boldsymbol{W_t}$

The ejection work of coal refers to the energy required when coal is projected from the coal wall into the tunnel.

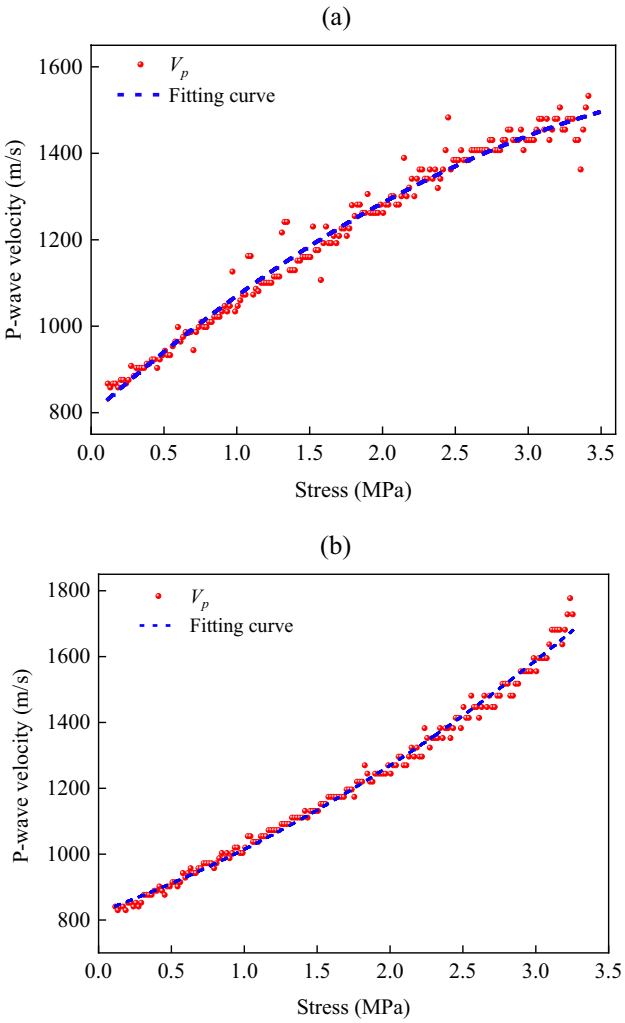

Fig. 6 Curve of longitudinal wave velocity versus stress. **a** Sample M1; **b** Sample M2

The ejection work per unit mass of coal can be approximately calculated using the following formula (Wu et al 2020):

$$W_t = \frac{mv^2}{2} = \frac{abx_p\rho v^2}{2} \tag{26}$$

where, v is the velocity that the coal powder has when it is thrown, usually take 1~5 m/s.

In summary, the energy dissipation ratio (R) serves as an indicator for identifying CGO hazard. The calculation formula for the R-value is presented in equation (27). When $R>1$ indicates that the tunneling roadway satisfies the energy condition for CGO.

$$R=\frac{E_e + E_g}{W_c + W_t} \tag{27}$$

3.2 NEDAS detection method

The mechanical model presented above emphasizes the significance of studying the hazard of CGO while considering the influence of NEDSA. Obtaining the NEDSA distribution is the basis for predicting the risk of CGO under stress anomalies. As a new geophysical method, seismic wave tomography imaging technology is widely used in engineering and geological diagnosis. It monitors the travel time and energy of seismic waves passing through geological bodies, and reconstructs the internal structure image of geological bodies through the organic combination of monitoring data and computer imaging technology, so as to realize the detection of wave velocity field in coal seam area. Previous research has confirmed that changes in stress cause the propagation speed of longitudinal waves in coal seams to vary (Chen et al. 2015). The inversion of longitudinal wave velocity distribution characteristics of coal seams by seismic wave tomography imaging, combined with the relationship between stress anomalies and wave velocity anomalies, can achieve the distribution acquisition of NEDSA in coal rock layers. Figure 5 shows the schematic diagram of the inversion principle, and the specific principle is shown in the studies of Cao et al (2015) and Luxbacher et al (2008).

The coupling relationship between wave velocity and stress can be obtained through laboratory experiments. Based on the wave velocity test method of zhao et al (2023), the wave velocity measurement test of 22# coal seam sample in Jinjia Coal Mine, Guizhou Province was carried out under uniaxial loading, and the results are shown in Fig. 6. It can be seen that the longitudinal wave velocity increases with the increase of stress, and the two are positively correlated. Based on the average load load of the sample before failure and the average wave velocity of the coal body during loading, we can calculate Stress anomaly coefficient β and wave velocity anomaly coefficient ξ, and analyze that the

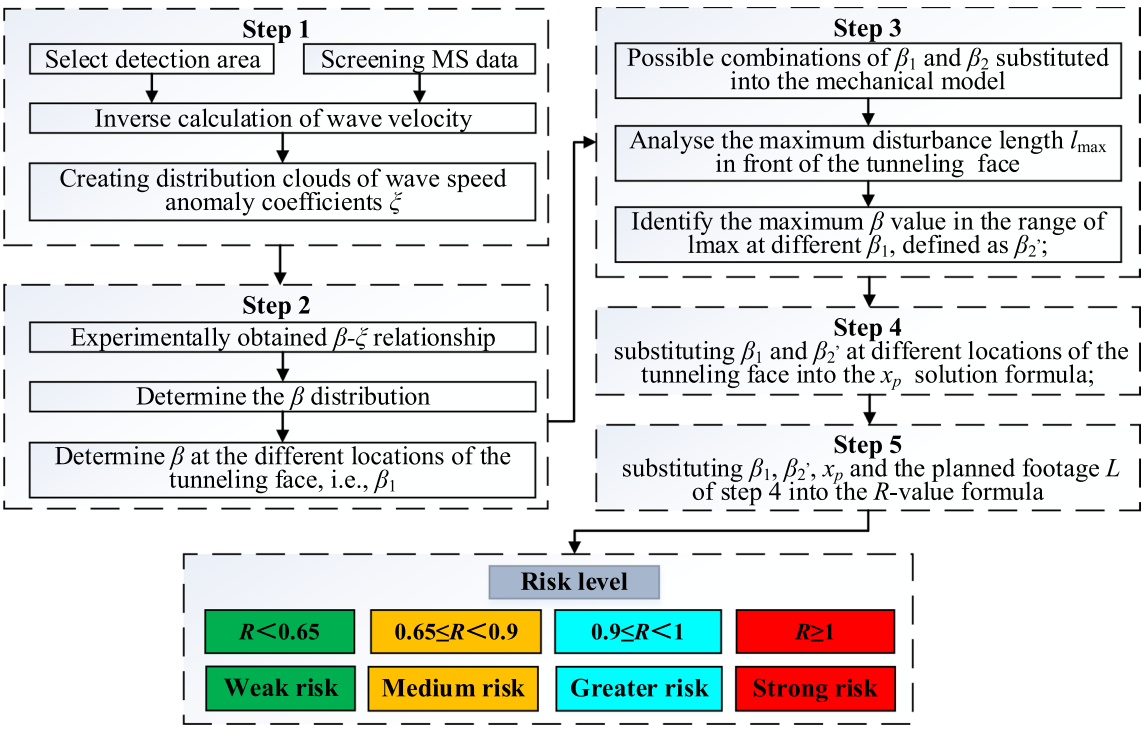

Fig. 7 Flow chart of CGO hazard prediction method

Table 1 Main parameters of coal seams

q (MPa)	σ_c (MPa)	φ (°)	λ	α	c_c	μ	p_1 (MPa)	f	P_0 (MPa)
11.7	3.2	16	0.75	0.1	0.15	0.43	0.1	0.1	0.7

Table 2 Calculated parameters of energy conversion

E (MPa)	T (K)	M (kg/kmol)	f	S_b (cm^2/g)	η	n	ρ (t/m^3)	v (m/s)	R_g (kJ/kg·K)	v_m (m^3/kmol)
1820	298.15	16	0.68	110	8.04	1.31	1.54	3	0.527	22.4

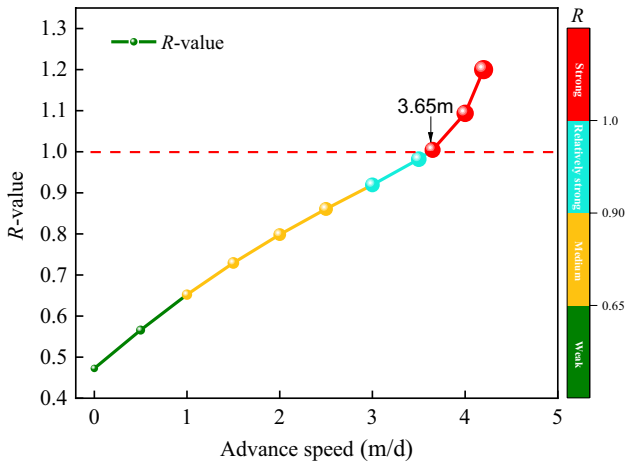

Fig. 8 R value of outburst hazard prediction index at different advancing speeds (No NEDSA)

proportional relationship between ξ and β is about 0.65, that is, $\beta = \xi/0.65$.

3.3 CGO prediction method

Based on the mentioned calculation formula for the CGO hazard R-value, it is evident that β_1、β_2、x_p, and the planned footage L are all unknown parameters. The parameters can be obtained through the NEDSA identification method and the established mechanical model calculation mentioned above. Therefore, the CGO hazard prediction method for excavation tunnels is as follows:

Step 1: To initiate the process, meticulously select the stress field detection area and curate an extensive dataset comprising over 50 MS monitoring data from this specific region within the last 10–20 days. Subsequently, leverage seismic wave tomography inverse calculations to ingeniously generate an intricate cloud map, revealing the distribution

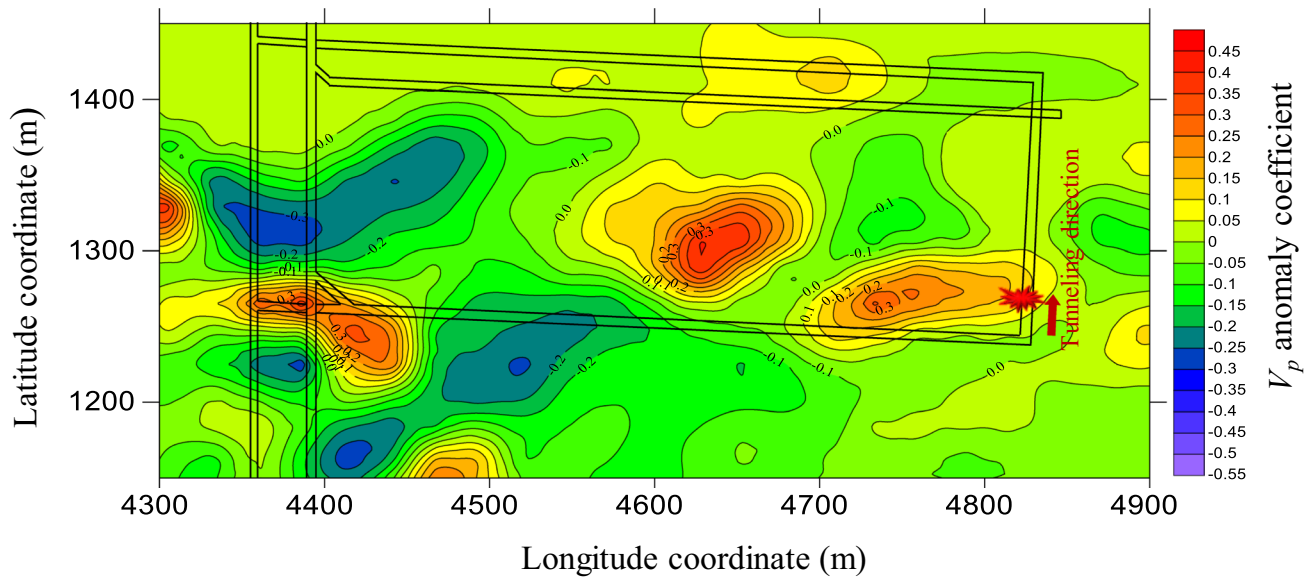

Fig. 9 The vibration wave velocity anomaly coefficient cloud map

Table 3 Wave velocity and stress anomaly coefficient in front of working face

Distance from working face (m)	Wave velocity anomaly coefficient	Stress anomaly coefficient
0 ~ 10	0	0
10 ~ 22	0.1	0.154
22 ~ 46	0.15	0.231
46 ~ 57	0.1	0.154

of wave velocity anomaly coefficients ξ, offering invaluable insights into the area's stress dynamics;

Step 2: Experimentally determine the relationship between the coal seam anomaly coefficient ξ and β (NEDSA coefficient). Subsequently, analyze the distribution of β and, based on the tunneling plan, identify β_1 values at different positions along the tunneling face.

Step 3: Substitute the possible combinations of β_1 and β_2 into the mechanical model, and determine the maximum value of β within the l_{max} (the maximum disturbance length in front of the tunneling head) range for different β_1 values. This maximum value is defined as β_2';

Step 4: Substitute β_1 and its corresponding β_2 at different positions in the driving face into the x_p solution formula to calculate x_p;

Step 5: Substitute β_1, β_2', x_p, and the planned penetration L from the fourth step into the R-value calculation formula. By doing so, we can calculate the R-value and determine the CGO danger level when the tunneling head is driven to different positions. The schematic diagram of the CGO prediction method is shown in Fig. 7.

3.4 Field application and verification

When the working face is advancing, the parameters required for the calculation of coal and gas protrusion danger prediction index R are shown in Tables 1 and 2. According to the Eqs. (2, 17, 18, 22, 24–27), we can calculate the coal and gas protrusion danger under different advancing speeds when there is no NEDSA, and the results are shown in Fig. 8. It can be seen that the protrusion danger enhances with the increase of mining speed when other conditions remain unchanged. The working face can take care of both production and safety at the same time when the digging speed is 1 ~ 3 m/d, and the maximum daily advancing speed should not exceed 3.65 m/d.

In this study, an MS monitoring system was installed on the 11224 working face of the 22# coal seam in the first mining area of the Jinjia coal mine. Before the excavation of the open-off cut, 62 MS data points were screened and used for seismic wave tomography inverse calculation. The resulting cloud map displaying the distribution of wave velocity anomaly coefficient is presented in Fig. 9.

Based on Fig. 9, we extracted the wave velocity anomaly coefficients at different distances from the working face and converted them into stress anomaly coefficients and the results are shown in Table 3. We observed that within the range of 0-10 m, 10-22 m, 22-46 m, and 46-57 m in front of the driving face, the abnormal coefficients of wave velocity are 0, 0.1, 0.15, and 0.1, respectively. The converted NEDSA coefficients are 0, 0.154, 0.231, and 0.154, respectively. Therefore, the possible combinations of β_1 and β_2 are as follows: (0, 0.154), (0, 0.231), (0.154, 0.231), (0.154, 0.154), (0.231, 0.231), (0.231, 0.154), (0.231, 0), and (0.154, 0). According to the stress calculation formula of elastic zone, plastic zone and original rock stress zone in Sect. 3.1, by substituting the combination of β_1 and β_2 into Eqs. (6), (9) and (14) in the above mechanical model, we can obtain the

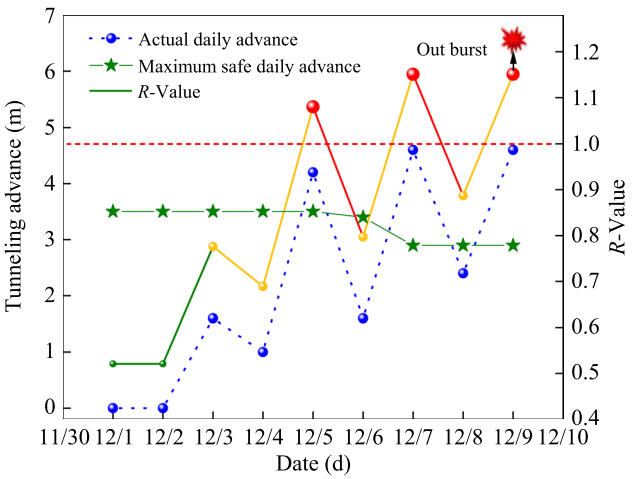

Fig. 10 CGO hazard prediction results

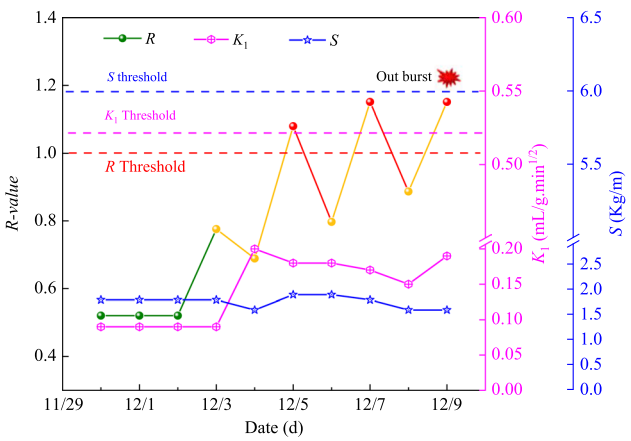

Fig. 11 Comparison of R indicators with K_1 and S indicators

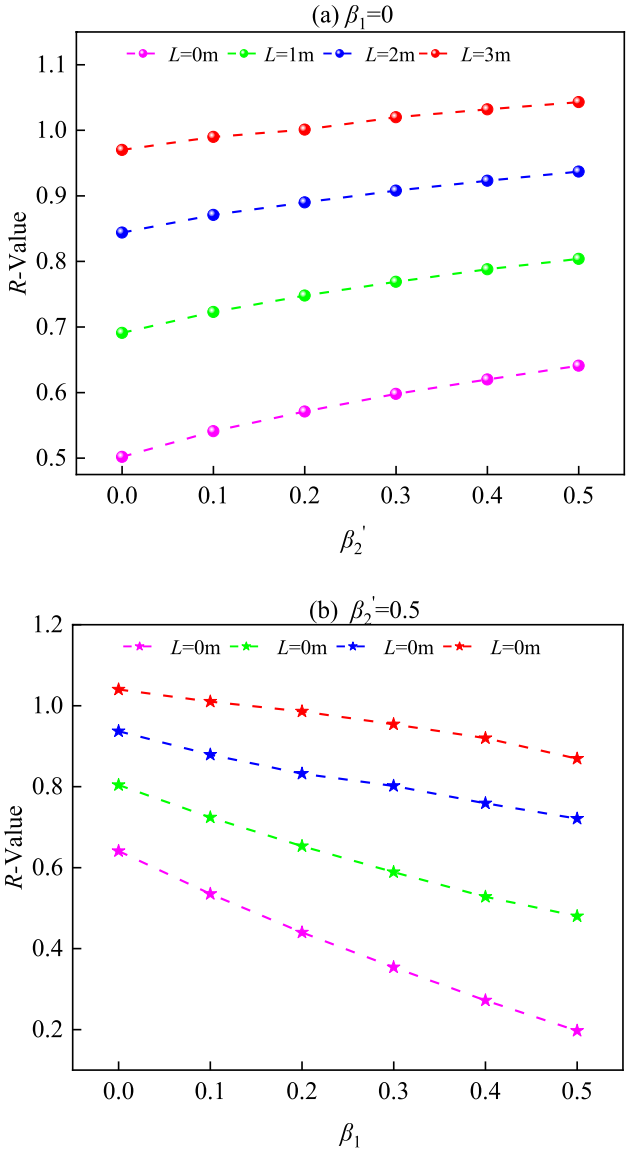

Fig. 12 Relationship between NEDSA gradient and CGO hazard in excavation roadway. **a** $\beta_1=0$, β_2 increased; **b** $\beta_2=0.5$, β_1 increased

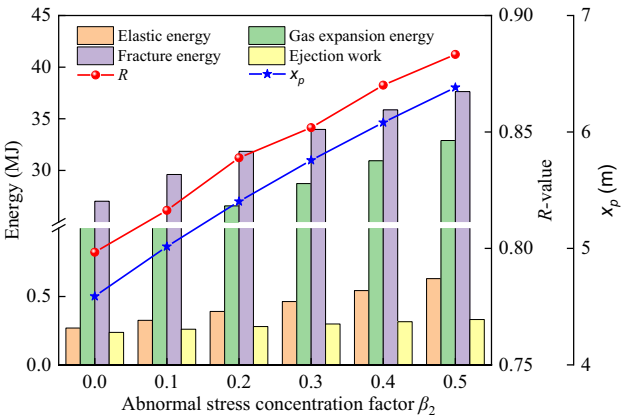

Fig. 13 Relationship between *R*-Value and various energy levels, and x_p as the NEDSA gradient increases

stress distribution under the stress anomaly, whose maximum perturbation length (l_{max}) is about 12 m.

The actual excavation length for the open-off cut from December 2nd to 9th is as follows: 0 m, 1.6 m, 1 m, 4.2 m, 1.6 m, 4.6 m, 2.4 m, and 4.6 m, respectively. According to the actual excavation length, the corresponding β_2' values for different positions of the driving face are 0.154, 0.154, 0.154, 0.154, 0.231, 0.231, and 0.231, respectively. The (β_1, β_2') combinations are divided into two categories: (0, 0.154) and (0.154, 0.213). Substituting these (β_1, β_2') values into the x_p calculation formula yields x_p values of 5.2 m and 5.5 m, respectively. When placing the driving face at different positions (β_1, β_2', x_p, *L*) into the *R*-value calculation formula, the predicted CGO hazard is shown in Fig. 10.

When $R=1$, we can back-calculate the daily advancing speed of the working face by associating Eqs. (2) (17) (18) (22) (24)~(27) to get the daily advancing speed of the working face, which we define as the maximum safe advance. As per the predictions on December 5th, December 7th, and December 9th, strong CGO hazards were identified. On December 9th, while conducting on-site tracking and monitoring, a minor CGO accident took place in the open-off cut area. Comparing the maximum safe footage in Fig. 10 with the actual footage, it indicates that no safety accidents occurred during on-site operations within the daily maximum safe advance speed. However, CGO accidents occurred when the excavation length exceeded the maximum allowable excavation length. Therefore, we can utilize the CGO hazard prediction method established in this paper to scientifically and effectively guide the daily advancement speed on site, thus reducing the CGO hazard.

The comparison results between the CGO prediction *R*-value index proposed in this article and the traditional drilling cuttings gas desorption index K_1 and drilling cuttings quantity *S*-value prediction index are shown in Fig. 11. It can be observed that after December 14th, K_1 and *S* values showed a slight increase and fluctuation, however, they remained significantly below the dangerous critical value. Compared to traditional indicators, the prediction results in this article demonstrate higher sensitivity and accuracy. CGO hazard prediction can be performed based on the planned daily excavation length after completing NEDSA detection. This effectively resolves the short lead time issue in traditional indicator prediction, which lacks enough time to implement local prevention and control measures and adjust excavation operation plans.

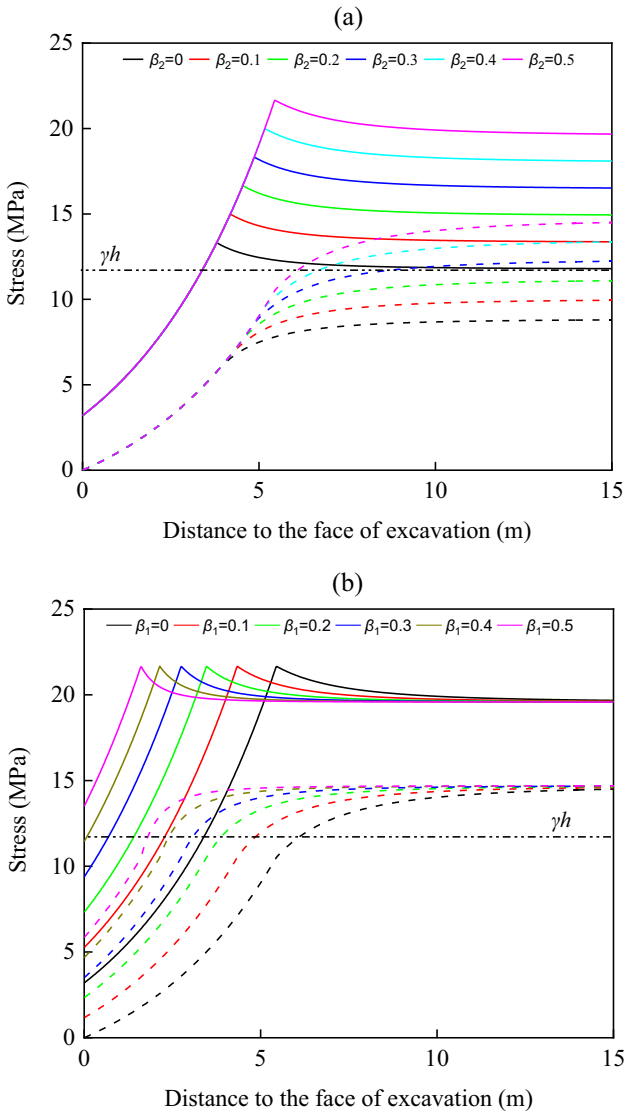

Fig. 14 Stress distribution in front of excavation work under different gas pressures. **a** $\beta_1=\beta_2=0$; **b** $\beta_1=0.1$, $\beta_2=0.5$

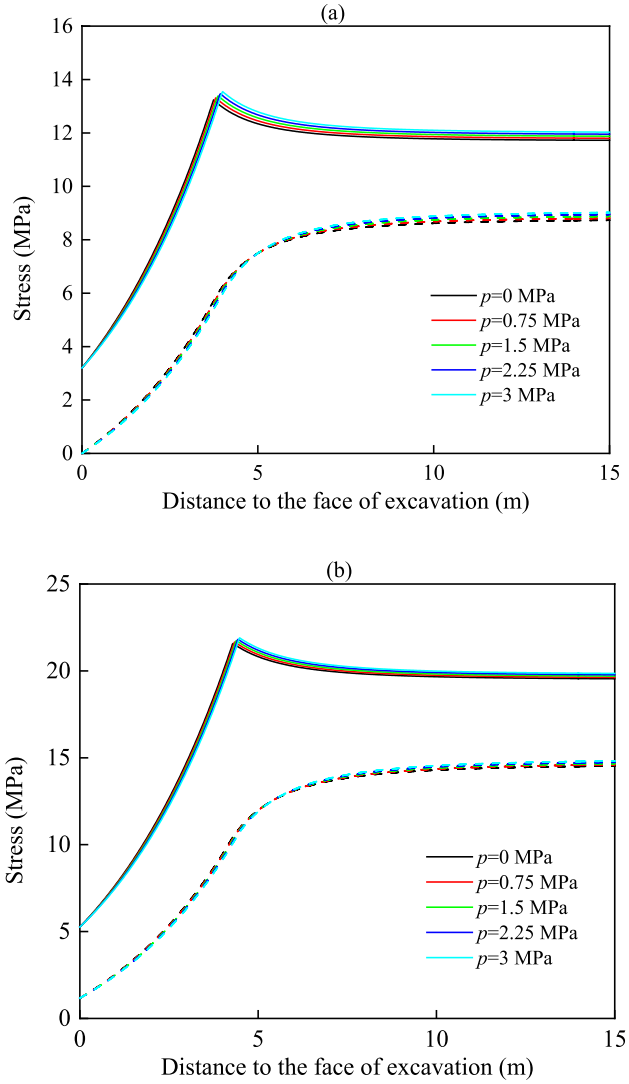

Fig. 15 Stress distribution in front of excavation work under the influence of NEDSA. **a** $\beta_2>0$, $\beta_1=0$; **b** $\beta_1>0$, $\beta_2=0.5$

4 Discussion

4.1 Mechanism of NEDSA's impact on CGO

The on-site application of the CGO hazard prediction method established in this article demonstrates its accurate forecasting of the CGO hazard during coal roadway driving. Taking coal seam 11,224 as an example, the CGO hazard during coal roadway driving was compared and analyzed under low gas pressure for different combinations of (β_1, β_2', L) using the CGO hazard prediction method developed in Sect. 3.4. The results are illustrated in Fig. 12. The results indicate that, under the same footage, the R-value is positively correlated with β_2' when β_1 is kept constant. Conversely, when β_2' is held constant, R-value negatively correlates with β_1.

Figure 13 illustrates the relationship among energy proportion, R-value, and x_p of the coal seam under different NEDSA when the excavation length is 2 m. As the NEDSA gradient increases, the value of R also increases. The changing trend of x_p closely follows that of R. From an energy perspective, the elastic energy accounts for 1.2% to 1.9% of the gas expansion energy, with a magnitude difference of approximately 50–100 times, which is in line with the findings of Zheng et al. (2004) that gas expansion energy is the primary source of CGO.

The analysis above can be summarized as follows: for the same excavation footage, there is a positive correlation between the NEDSA gradient in front of the excavation face and the CGO hazard R-value, and the R-value is also

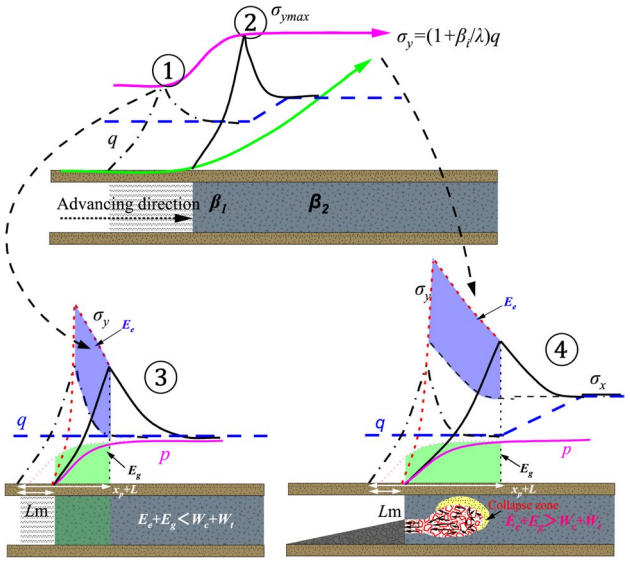

Fig. 16 Schematic diagram of NEDSA's influence mechanism on CGO excitation

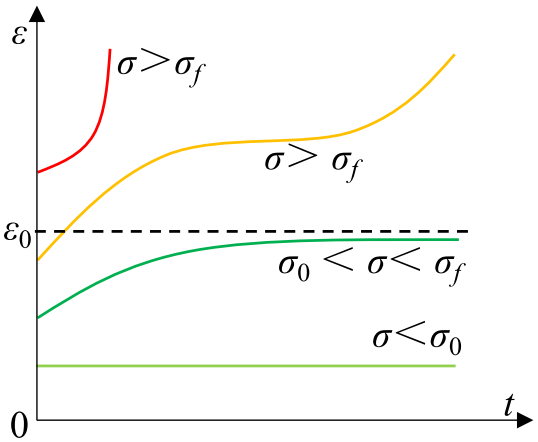

Fig. 17 Creep curves under different stresses

positively correlated with x_p. The effects of NEDSA and gas on the length of the plastic zone were analyzed and presented in Figs. 14 and 15. It is evident that an increase in the NEDSA gradient leads to higher values of x_p and vertical peak stress. Gas has a negligible impact on x_p and vertical peak stress compared to NEDSA.

Therefore, this article posits that NEDSA primarily influences CGO excitation through two aspects. Firstly, the increase in NEDSA gradient results in greater gas involvement in CGO excitation. As shown in Fig. 16, The larger the stress anomaly gradient within the disturbance range in front of the coal wall, the longer the length x_p of the plastic zone in front of the working face, indirectly leading to an increase in the released gas internal energy and an increased risk of CGO.

On the other hand, when NEDSA affects the front of the working face, the peak stress increases. After excavation, the coal body in the elastic zone transitions from an elastic state to a plastic state to achieve a new equilibrium. During this process, high peak stress accelerates coal failure, triggering a chain reaction of coal destruction, gas release, and further coal destruction, resulting in a higher CGO hazard. This is consistent with Zhou et al. 's conclusion that increased geological stress significantly increases the release of gas expansion energy in the CGO process (Zhou et al 2020).

4.2 Accuracy of CGO disaster prediction indicator

On-site verification indicates no CGO accidents when the excavation face first reached a position with $R>1$; however, a CGO occurred when it reached a position with $R>1$ for the third time. This is primarily attributed to the following reasons: Firstly, the CGO hazard, as characterized by the R-value in this paper, entails the rapid release of energy and the swift establishment of a new stress equilibrium. However, the release of energy requires a process and experiences a certain lag. Additionally, coal exhibits rheological mutation characteristics, and CGO disasters undergo a gradual evolution process, transitioning from slow rheological to rapid rheological behavior.

Figure 17 depicts the rheological curve of coal and rock mass under various stress states (Wang et al. 2009). A small NEDSA gradient causes the coal to flow slowly, leading to the early release of some energy, resulting in an actual $R<1$. Nevertheless, in the context of CGO prevention and control, even when considering the influence of time effect and coal flow, it remains crucial to remain vigilant about the high hazard of CGO disasters when $R>1$. The CGO hazard prediction method proposed in this article enables the prediction of CGO hazards during the incubation stage, advancing the hazard prediction timeline and providing ample time for on-site prevention and control measures to ensure personnel safety during operations. Meanwhile, studies indicate that coal and rock mass damage occur under high stress, leading to intensified acoustic emission and electromagnetic radiation signals (Zhao et al 2022). To enhance disaster prevention and control capabilities, real-time monitoring of the local stress state in front of the coal body can be achieved using acoustic emission and electromagnetic radiation equipment, thereby augmenting the timeliness of CGO hazard prediction.

5 Conclusions

In this paper, we unveil a meticulously crafted mechanical model for coal roadways with gas bearings, thoughtfully incorporating the influence of non-excavation disturbance stress anomaly (NEDSA). Our comprehensive study delves into the critical factors that trigger coal and gas outburst (CGO) incidents, laying the foundation for a robust CGO hazard prediction method, expertly designed based on NEDSA detection. Our method was rigorously tested and validated through on-site engineering, affirming its efficacy and real-world applicability. Furthermore, the influence mechanism of NEDSA on CGO and the accuracy of the prediction index R were also discussed. The conclusion is as follows:

(1) The improved limit equilibrium model established in this paper can simultaneously consider the influence of NEDSA gradient and gas on roadway stress. The greater the NEDSA gradient, the greater the x_p, and the higher the vertical peak stress. The influence of gas on x_p and vertical stress is nearly negligible.
(2) The NEDSA gradient in front of the excavation face positively correlates with the CGO hazard R-value under the same footage. NEDSA impacts the hazard of CGO through two mechanisms. Firstly, it alters the length of the plastic zone x_p, which affects the amount of gas involved in CGO excitation. Secondly, it influences the vertical stress magnitude, leading to changes in the chain reaction rate of coal failure, gas release, and subsequent coal failure.
(3) On-site verification has unequivocally affirmed the outstanding precision of our predictions, as all three major protruding hazardous locations were accurately identified, with one of them experiencing a minor CGO incident. By effectively addressing the limitations of traditional prediction indicators, our method provides ample lead time, affording the opportunity for prompt implementation of localized prevention and control measures, as well as timely adjustments to mining operation plans.

Acknowledgements This work was financially supported by the National Natural Science Foundation of China (52174162), and the Fundamental Research Funds for the Central Universities (FRF-TP-20-002A3).

Author contributions Yingjie Zhao: Conceptualization, formal analysis, investigation, validation, writing—original draft. Dazhao Song: Methodology, conceptualization, writing—review & editing, funding acquisition, supervision. Liming Qiu: writing—review & editing, supervision. Xueqiu He: Writing—review & editing. Zhenlei Li: Methodology, funding acquisition, writing—review & editing. Yujie Peng: Funding acquisition, writing—review & editing. Anhu Wang: Software, investigation.

Funding National Natural Science Foundation of China, 52174162, Dazhao Song, Fundamental Research Funds for the Central Universities, FRF-TP-20-002A3, Dazhao Song.

Availability of data and materials The data generated and/or analyzed during the current study are not publicly available for legal/ethical reasons but are available from the corresponding author on reasonable request.

Declarations

Competing interest The authors declare that they have no known competing financial interests.

References

An FH, Yuan Y, Chen XJ, Li ZQ, Li LY (2019) Expansion energy of coal gas for the initiation of coal and gas outbursts. Fuel 235:551–557. https://doi.org/10.1016/j.fuel.2018.07.132

Black DJ (2019) Review of current method to determine outburst threshold limits in Australian underground coal mines. Int J Min Sci Technol 29(6):859–865. https://doi.org/10.1016/j.ijmst.2019.03.002

Cai CG, Xiong YX (2005) Theoretical and experimental study on crushing energy of outburst-proneness coal. J China Coal Soc 30(1):63–66. https://doi.org/10.3321/j.issn:0253-9993.2005.01.014

Cao AY, Dou LM, Cai W, Gong SY, Liu S, Jing GC (2015) Case study of seismic hazard assessment in underground coal mining using passive tomography. Int J Rock Mech Min Sci 78:1–9. https://doi.org/10.1016/j.ijrmms.2015.05.001

Cao J, Dai L, Sun H, Wang B, Zhao B, Yang X, Zhao X, Guo P (2019) Experimental study of the impact of gas adsorption on coal and gas outburst dynamic effects. Process Saf Environ Prot 128:158–166. https://doi.org/10.1016/j.psep.2019.05.020

Chen TJ, Wang X, Mukerji T (2015) In situ identification of high vertical stress areas in an underground coal mine panel using seismic refraction tomography. Int J Coal Geol 149:55–66. https://doi.org/10.1016/j.coal.2015.07.007

Chen LL, Wang YQ, Ma EL, Wang ZF (2023) Failure analysis and countermeasures of highway tunnel crossing fault fracture zone in coal-bearing strata: a case study. Eng Fail Anal 143:106800. https://doi.org/10.1016/j.engfailanal.2022.106800

Jia SC, Wang JC, Zhu JM (2011) Calculation and application on elastic-plastic coal pillar width of the stope. Procedia Eng 26:1116–1124. https://doi.org/10.1016/j.proeng.2011.11.2282

Jiang CL, Yu QX (1998) Mechanisms and Control Technologies of Coal and Gas Outburst in Spherical Shells Destabilization. China University of Mining and Technology Press, Xuzhou

Kong B, Cao ZY, Sun T, Qi CX, Zhang Y (2022) Safety hazards in coal mines of Guizhou China during 2011–2020. Saf Sci 145:105493. https://doi.org/10.1016/j.ssci.2021.105493

Li H, Feng ZC, Zhao D, Duan D (2017) Simulation experiment and acoustic emission study on coal and gas outburst. Rock Mech Rock Eng 50(8):2193–2205. https://doi.org/10.1007/s00603-017-1221-3

Li W, Ren TW, Busch A, den Hartog SAM, Cheng YP, Qiao W, Li B (2018) Architecture, stress state and permeability of a fault zone in Jiulishan coal mine, China: implication for coal and gas outbursts. Int J Coal Geol 198:1–13. https://doi.org/10.1016/j.coal.2018.09.002

Li P, Cai MF, Guo QF, Ren FH, Miao SJ (2022) Current stress field and its relationship to tectonism in a coal mining district, central China, for underground coal energy exploration. Energy Rep 8:5313–5328. https://doi.org/10.1016/j.egyr.2022.04.008

Liu T, Lin BQ, Fu XH, Liu A (2021) Mechanical criterion for coal and gas outburst: a perspective from multiphysics coupling. Int J Coal Sci Technol 8(6):1423–1435. https://doi.org/10.1007/s40789-021-00447-z

Lu SQ, Li L, Cheng YP, Sa ZY, Zhang YL, Yang N (2017) Mechanical failure mechanisms and forms of normal and deformed coal combination containing gas: model development and analysis. Eng Fail Anal 80:241–252. https://doi.org/10.1016/j.engfailanal.2017.06.022

Luxbacher K, Westman E, Swanson P, Karfakis M (2008) Three-dimensional time-lapse velocity tomography of an underground longwall panel. Int J Rock Mech Min Sci 45(4):478–485. https://doi.org/10.1016/j.ijrmms.2007.07.015

Pan XK, Cheng H, Chen J, Zhou XP (2020) An experimental study of the mechanism of coal and gas outbursts in the tectonic regions. Eng Geol 279:105883. https://doi.org/10.1016/j.enggeo.2020.105883

Peng SJ, Xu J, Yang HW, Liu D (2012) Experimental study on the influence mechanism of gas seepage on coal and gas outburst disaster. Saf Sci 50(4):816–821. https://doi.org/10.1016/j.ssci.2011.08.027

Qian MG, Shi WP, Xu JL (2003) Mine pressure and rock formation control. China University of Mining and Technology Press, Xuzhou

Shu LY, Yuan L, Li QX, Xue WT, Zhu NN, Liu ZS (2023) Response characteristics of gas pressure under simultaneous static and dynamic load: implication for coal and gas outburst mechanism. Int J Min Sci Technol 33(2):155–171. https://doi.org/10.1016/j.ijmst.2022.11.005

Sobczyk J (2014) A comparison of the influence of adsorbed gases on gas stresses leading to coal and gas outburst. Fuel 115:288–294. https://doi.org/10.1016/j.fuel.2013.07.016

Soleimani F, Si GY, Roshan H, Zhang J (2023a) Numerical modelling of coal and gas outburst initiation using energy balance principles. Fuel 334:126687. https://doi.org/10.1016/j.fuel.2022.126687

Soleimani F, Si G, Roshan H, Zhang J (2023b) Numerical modelling of gas outburst from coal: a review from control parameters to the initiation process. Int J Coal Sci Technol 10(1):35–81. https://doi.org/10.1007/s40789-023-00657-7

Tian XH, Song D, He XQ, Li ZL, Liu HF, Wang WX (2021) Investigation on micro-surface adhesion of coals and implications for gas occurrence and coal and gas outburst mechanism. J Nat Gas Sci Eng 94:104115. https://doi.org/10.1016/j.jngse.2021.104115

Wang EY, He XQ (2009) Coal and rock electromagnetic radiation technology and application. Science Press, Beijing

Wang L, Liu SM, Cheng YP, Yin GZ, Guo PK, Mou JH (2017) The effects of magma intrusion on localized stress distribution and its implications for coal mine outburst hazards. Eng Geol 218:12–21. https://doi.org/10.1016/j.enggeo.2017.01.002

Wang CJ, Yang SQ, Yang DD, Li XW, Jiang CL (2018a) Experimental analysis of the intensity and evolution of coal and gas outbursts. Fuel 226:252–262. https://doi.org/10.1016/j.fuel.2018.03.165

Wang G, Liu XL, Xu H, Wu MM, Wang R, Cao JJ (2018b) Study on gas-bearing coal seam destabilization based on the improved Lippmann model and stress wave theory. J Loss Prev Process Ind 56:334–341. https://doi.org/10.1016/j.jlp.2018.09.013

Wang AH, Song DZ, He XQ, Dou LM, Li ZL, Zu ZY, Lou Q, Zhao YJ (2019) Investigation of coal and gas outburst risk by microseismic monitoring. PLoS ONE 14(5):e216464. https://doi.org/10.1371/journal.pone.0216464

Wold MB, Connell LD, Choi SK (2008) The role of spatial variability in coal seam parameters on gas outburst behaviour during coal mining. Int J Coal Geol 75(1):1–14. https://doi.org/10.1016/j.coal.2008.01.006

Wu X, Peng YW, Xu J, Yan Q, Nie W, Zhang TT (2020) Experimental study on evolution law for particle breakage during coal and gas outburst. Int J Coal Sci Technol 7(1):97–106. https://doi.org/10.1007/s40789-019-00284-1

Xu T, Tang CA, Yang TH, Zhu WC, Liu J (2006) Numerical investigation of coal and gas outbursts in underground collieries. Int J Rock Mech Min Sci 43(6):905–919. https://doi.org/10.1016/j.ijrmms.2006.01.001

Xue S, Yuan L, Wang YC, Xie J (2014) Numerical analyses of the major parameters affecting the initiation of outbursts of coal and gas. Rock Mech Rock Eng 47(4):1505–1510. https://doi.org/10.1007/s00603-013-0425-4

Yu BH, Wang DM (2013) Research on dilatation energy of released gas from coal seam. J Min Saf Eng 5:773–777

Zhang S, Yang S, Cheng J, Zhang B, Lu C (2011) Study on relationships between coal fractal characteristics and coal and gas outburst. Procedia Eng 26:327–334. https://doi.org/10.1016/j.proeng.2011.11.2175

Zhang CL, Wang EY, Xu J, Peng SJ (2021) A new method for coal and gas outburst prediction and prevention based on the fragmentation of ejected coal. Fuel 287:119493. https://doi.org/10.1016/j.fuel.2020.119493

Zhao YJ, Song DZ, Wei MH, Khan M, Li ZL, Qiu LM, Yin S (2022) Analyzing the synchronous acoustic and electric response of coal burst failure: validation through the on-site application. Foundations 2(3):746–762. https://doi.org/10.3390/foundations2030051

Zhao YJ, He XQ, Song DZ, Qiu LM, Cheng XH, Li ZL, He SQ (2023) Identification of the relatively low permeability area in coal and gas outburst seams by seismic wave tomography technique: field application and validation. J Appl Geophys 210:104951. https://doi.org/10.1016/j.jappgeo.2023.104951

Zheng Z (2004) The mechanism of coal and gas outburst from the view of quantity and dimensional analysis. Collect Work Zheng Zhe min.

Zhou B, Xu J, Peng SJ, Yan FZ, Cheng L, Ni GH (2020) Influence of geo-stress on dynamic response characteristics of coal and gas outburst. Rock Mech Rock Eng 53(11):4819–4837. https://doi.org/10.1007/s00603-020-02154-8